

High-Potential Porphyrins Supported on SnO₂ and TiO₂ Surfaces for Photoelectrochemical Applications

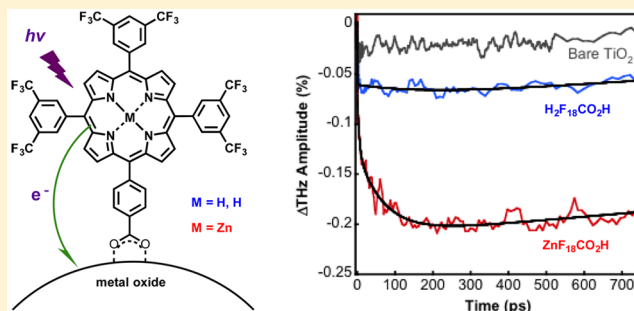
Jianbing Jiang, John R. Swierk, Kelly L. Materna, Svante Hedström, Shin Hee Lee, Robert H. Crabtree,* Charles A. Schmuttenmaer,* Victor S. Batista,* and Gary W. Brudvig*

Department of Chemistry, Yale University, New Haven, Connecticut 06520, United States

USA and Energy Sciences Institute, Yale University, West Haven, Connecticut 06516, United States

S Supporting Information

ABSTRACT: We report CF₃-substituted porphyrins and evaluate their use as photosensitizers in water-splitting dye-sensitized photoelectrochemical cells (WS-DSPECs) by characterizing interfacial electron transfer on metal oxide surfaces. By using (CF₃)₂C₆H₃ instead of C₆F₅ substituents at the meso positions, we obtain the desired high potentials while avoiding the sensitivity of C₆F₅ substituents to nucleophilic substitution, a process that limits the types of synthetic reactions that can be used. Both the number of CF₃ groups and the central metal tune the ground and excited-state potentials. A pair of porphyrins bearing carboxylic acids as anchoring groups were deposited on SnO₂ and TiO₂ surfaces, and the interfacial charge-injection and charge-recombination kinetics were characterized by using a combination of computational modeling, terahertz measurements, and transient absorption spectroscopy. We find that both free-base and metalated porphyrins inject into SnO₂ and that recombination is slower for the latter case. These findings demonstrate that (CF₃)₂C₆H₃-substituted porphyrins are promising photosensitizers for use in WS-DSPECs.



1. INTRODUCTION

Increasing concerns on greenhouse gases generated from fossil fuels have prompted the exploration of renewable energy resources. Solar energy has drawn significant attention because it is abundant, sustainable, and environmentally friendly. Several types of devices have been developed over the past few decades, including silicon-based photovoltaic panels, dye-sensitized solar cells (DSSCs), polymer solar cells, and perovskite solar cells.^{1–3} Here, we focus on photosensitizers for dye-sensitized photoelectrochemical cells for water splitting.

Photoelectrochemical dye-sensitized solar cells for water splitting are typically constructed with photoanodes consisting of mesoporous metal oxides functionalized with light-absorbing chromophores and water-oxidation catalysts. Under illumination, the chromophores are photoexcited and inject electrons into the conduction band of the metal oxide. The injected electrons then percolate through the mesoporous film until reaching the back contact and are transported to the cathode, where they reduce protons and generate H₂.⁴ The hole left behind in the photo-oxidized chromophore is transferred to a water-oxidation catalyst. The overall process is repeated four times before the catalyst is regenerated in its reduced form by water oxidation.

Central to cell performance are the light-absorbing chromophores that convert solar energy into an electrochemical potential and shuttle holes to the water-oxidation catalyst. Efficient cells require photosensitizers that absorb strongly in

the visible range of the solar spectrum, bear robust anchoring groups for binding to the semiconductor surface, have a ground-state potential sufficiently positive to facilitate hole transfer to the catalyst, have an excited-state potential more negative than the edge of the semiconductor conduction band to facilitate interfacial electron transfer (IET), and exhibit good thermo-, photo- and chemical stability.

A variety of photosensitizers have been utilized for DSSCs, including inorganic complexes, porphyrins, phthalocyanines, and other organic dyes. Compared to DSSCs, significantly fewer sensitizers have been demonstrated in photocatalytic cells, with phosphonated ruthenium(II) polypyridyls being the overwhelming choice,^{5–7} though porphyrins^{8–11} and organic sensitizers^{12,13} have attracted recent attention. Representative photosensitizer structures that were previously investigated are shown in Chart 1.^{11,14,15} Of the many types of sensitizers, porphyrins are highly attractive choices because they have a broad, tunable absorbance across the visible region, appropriate HOMO and LUMO energy levels for catalytic water oxidation, and high electrochemical and photochemical stability.¹⁶ Furthermore, widely studied porphyrin synthetic methodologies permit structural modifications that readily tune the photophysical and electrochemical properties.

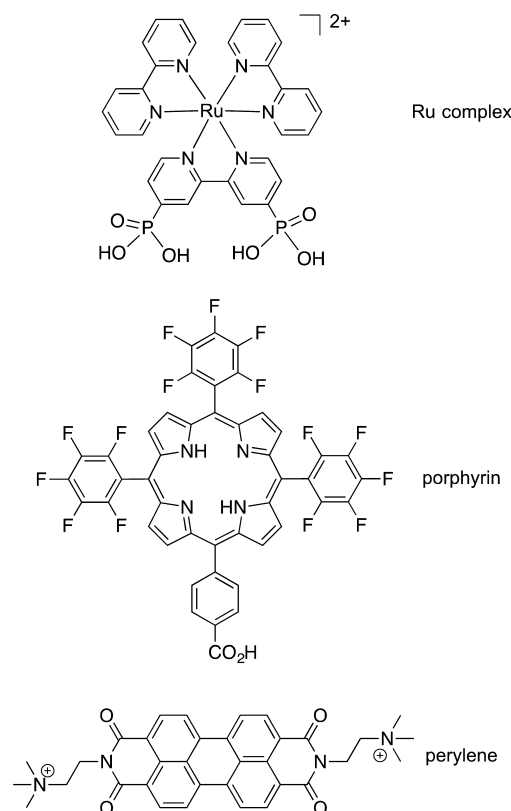
Received: October 13, 2016

Revised: November 26, 2016

Published: December 3, 2016



Chart 1. Representative Photosensitizers Previously Used



Redox potential tunability is critical for positioning the redox potential of the photosensitizer to match the potential of the coadsorbed catalyst and the semiconductor conduction band.¹⁷ A dominant methodology for preparing porphyrins with potentials high enough to enable water oxidation involves substitution of the meso or β -positions with electron-withdrawing groups to stabilize the frontier orbitals and raise the associated potentials. Pentafluorophenyl groups are widely used as electron-withdrawing units in the meso positions,^{18,19} whereas fluorine atoms, cyano groups, or nitro groups are commonly attached to the β positions.^{20–22} Incorporation of electron-withdrawing units to the porphyrin β -position entails extra synthetic steps, often requiring harsh reaction conditions. Another strategy for adjustment of the redox potentials is metalation,^{23,24} but some heavy metals promote spin–orbit coupling, leading to population of triplet excited states with lower driving force for IET.²³

A disadvantage of pentafluorophenyl groups is the vulnerability of the *para*-C–F group to nucleophiles^{25–31} that precludes some further derivatization routes for these molecules. Here, we demonstrate a simple strategy to synthesize trifluoromethylated porphyrins that behave analogously to high-potential, pentafluorophenyl porphyrins while avoiding the vulnerability to nucleophilic attack. Ten porphyrins that bear two to four bis(3,5-trifluoromethyl)phenyl groups were designed, synthesized, and characterized. Three zinc–metalated porphyrins were also used to fine-tune the redox potentials and spectral response. The electrochemical and photophysical properties were characterized by cyclic voltammetry, spectroscopy, and quantum chemistry calculations, providing insights into the geometry, electronic structure, energy level alignment, absorption/emission features, and redox potentials.

2. EXPERIMENTAL METHODS

2.1. Absorption and Emission Spectroscopies. The UV–visible absorption spectra were recorded on a Shimadzu UV-2600 UV–visible spectrophotometer. Fluorescence emission spectra were recorded on a Horiba Scientific FluoroMax Plus fluorophotometer. The UV–visible absorption and fluorescence emission spectra were collected for each porphyrin in dichloromethane at typical porphyrin concentrations of $\sim 0.2 \mu\text{M}$. The molar extinction coefficients were determined by measuring multiple spectra at a low concentration range of $0.05\text{--}0.5 \mu\text{M}$ in dichloromethane.

The excited-state (S_1) potentials were estimated by extracting the zero-excitation energy (E_{0-0}) from the ground-state potentials according to the Rehm–Weller approximation:³²

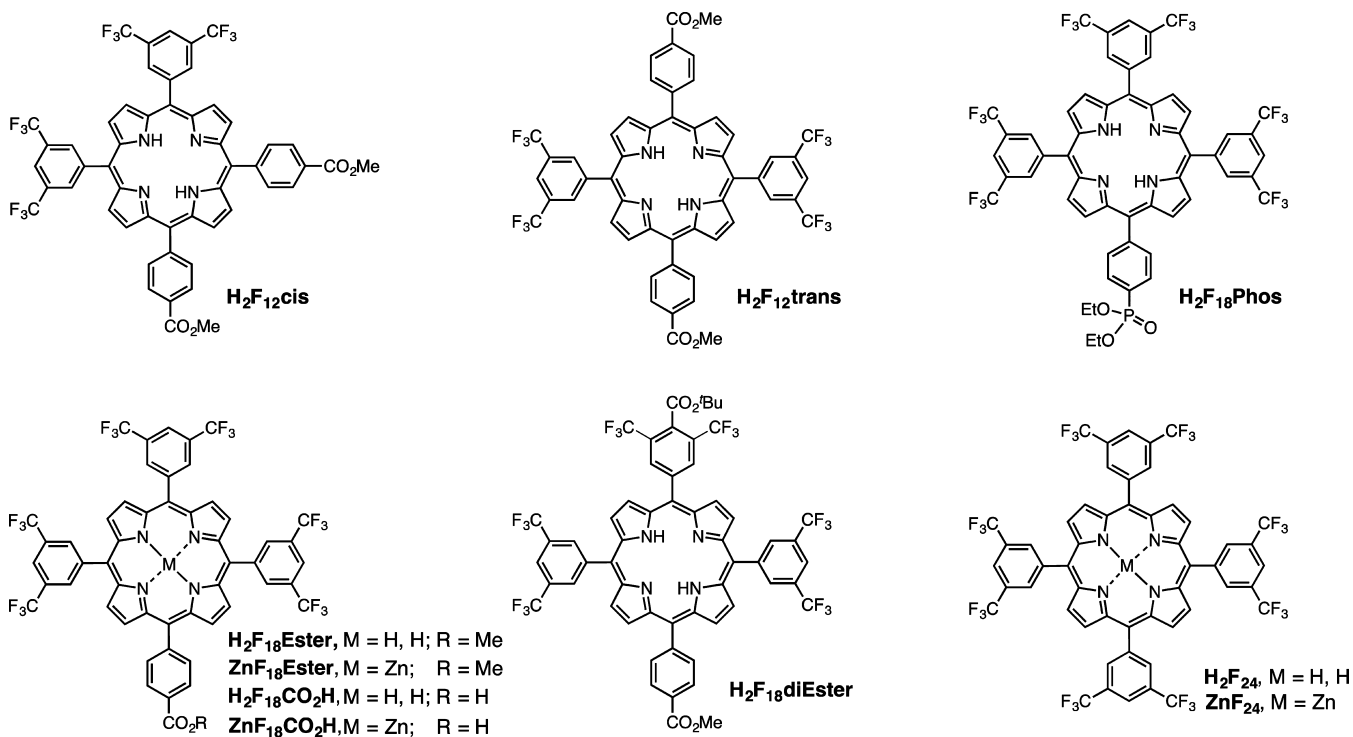
$$E^0(P^+/\cdot P) \approx E^0(P^+/P) - \frac{E^0(P \rightarrow \cdot P)}{e} \quad (1)$$

where $E^0(P^+/\cdot P)$ is the excited-state potential for the porphyrin radical cation/excited singlet state porphyrin couple, $E^0(P^+/P)$ is the ground-state potential for the porphyrin radical cation/porphyrin couple, $E_{0-0}(P \rightarrow \cdot P)$ is the estimated transition energy from the ground state to the porphyrin first excited singlet state, and e is the elementary charge of an electron.

2.2. Electrochemistry. Cyclic voltammetry (CV) experiments were performed on a Pine WaveNow potentiostat. A three-electrode electrochemical cell configuration was used, incorporating a glassy carbon working electrode, a Ag/AgCl pseudoreference electrode, and a platinum wire auxiliary electrode. Tetrabutylammonium hexafluorophosphate (TBAPF₆) was recrystallized twice prior to use, and 0.10 M TBAPF₆ in dichloromethane was the supporting electrolyte. The glassy carbon electrode was polished between cyclic voltammograms with an alumina slurry on a polishing pad. The concentration of the porphyrins was $\sim 3 \text{ mM}$ for the CV measurements. The ferrocenium/ferrocene redox couple was used as an internal standard to establish the potential of the pseudoreference electrode, and the ferrocenium/ferrocene $E_{1/2}$ is 0.690 V vs NHE in dichloromethane.³³ All CVs are referenced to NHE and were taken with a scan rate of 50 mV/s. The absorption spectra of the radical cations were collected via controlled potential electrolysis using a 0.1 M TBAPF₆ electrolyte in dichloromethane with a platinum flag high surface area working electrode, an Ag/AgCl pseudoreference electrode, and a platinum auxiliary electrode.

2.3. Quantum Chemistry Calculations. All calculations were performed with the Gaussian09 Revision D.01 software³⁴ using a polarizable continuum model (PCM) of the dichloromethane solvent.³⁵ The porphyrins H₂F₁₈Ester, H₂F₁₈Phos, H₂F₁₈diEster, and ZnF₁₈Ester were optimized in their ground, reduced, and oxidized states at the density functional theory (DFT) PBE0/6-31G(df,p) level of theory.³⁶ Vibrational frequency calculations were performed to ensure that a stationary point with no imaginary frequencies was reached upon optimization. Energies and electronic structures were obtained from subsequent single point calculations using the 6-311+G(df,p) basis set. The excited states were interrogated with linear-response time-dependent (TD)-DFT, including calculations of vertical transitions from the ground-state geometry and relaxed configuration in the S_1 excited state. TD-DFT calculations were performed at the CAM-B3LYP/6-31G(d) level, which was previously shown to be suitable for porphyrin excited-state calculations.^{37,38} Additional ground-

Chart 2. Structures of Ten Trifluoromethylated Porphyrins



state optimizations were performed at this level of theory for comparison of geometries in the S_0 and S_1 states.

2.4. Time-Resolved Terahertz (THz) Spectroscopy. The experimental technique and specific instrumentation for time-resolved THz spectroscopy (TRTS) measurements are described in detail elsewhere.^{39–43} Briefly, the 800 nm output of an amplified Ti:sapphire laser (Spectra Physics, 35 fs pulse, 1 kHz repetition) is split into three beams. One beam is used to generate THz radiation by frequency doubling, and then both the fundamental and second harmonic are focused in air to generate a plasma.^{44,45} The forward propagating THz radiation generated by the plasma is collected and focused using off-axis paraboloidal mirrors. The pump beam is frequency doubled to 400 nm, and the power is subsequently attenuated to 100 mW/cm² (6 mm diameter spot) with a variable neutral density filter. Finally, the THz radiation is detected using free-space electro-optic sampling with a ZnTe(110) crystal.⁴⁶

The TRTS scans were fitted with the following function:

$$\Delta\text{THz} = \left\{ \Delta\text{THz}_0 + \sum_{i=1}^n A_i \left[\exp\left(\frac{t-t_0}{\tau_i}\right) - 1 \right] \right\} \otimes G(\text{FWHM}) \quad (2)$$

where ΔTHz_0 is the baseline before $t = 0$, n is the number of exponentials included in the fit, t_0 corresponds to the injection time (i.e., $t = 0$), A_i is the amplitude of a given component, τ_i is the lifetime of a given component, $G(\text{FWHM})$ is a Gaussian instrument response function (determined to be 0.5 ps), and \otimes represents a convolution.

TiO₂ and SnO₂ films were prepared and sealed with 0.1 M Na₂SO₄ (aq), as previously described.⁴⁰ The films for TRTS study were sensitized by soaking in a 0.1 mM solution of ZnF₁₈CO₂H or H₂F₁₈CO₂H in CHCl₃ for 22 h at room temperature.

2.5. Transient Absorption Studies. ZnF₁₈CO₂H or H₂F₁₈CO₂H was deposited on ~ 2 μm -thick films of TiO₂ or SnO₂ from 0.5 mM solutions of ZnF₁₈CO₂H or H₂F₁₈CO₂H at 90 °C in toluene. Samples were measured in 0.1 M Na₂SO₄ (aq, pH 6) as well as on bare TiO₂ and SnO₂. Nanosecond transient absorption measurements were performed using an Edinburgh Instruments LP920 transient absorbance spectrometer. ZnF₁₈CO₂H and H₂F₁₈CO₂H were photoexcited at 530 and 505 nm (5 mJ/pulse, 7 ns, 10 mm diameter) using an OPO (Spectra-Physics basiScan M) pumped by the third harmonic of a Nd:YAG laser (Spectra-Physics INDI-10). A pulsed 450 W Xe arc lamp was utilized as the probe source. Various filters were placed after the sample to remove scattered laser light, and the probe light was passed through a monochromator and detected using a photomultiplier tube.

3. RESULTS AND DISCUSSION

3.1. Molecular Designs. The set of ten trifluoromethylated (CF₃) porphyrins was prepared, bearing different functional groups (mono- and dicarboxylates and phosphonate), geometries (A_3B -, cis - A_2B_2 -, $trans$ - A_2B_2 -, and $trans$ - A_2BC -types) and numbers of electron-withdrawing groups (12, 18, or 24 fluorine atoms) (Chart 2), including two benchmark molecules (H₂F₂₄ and ZnF₂₄), six porphyrin-ester precursors (H₂F₁₈Ester, ZnF₁₈Ester, H₂F₁₈Phos, H₂F₁₂cis, H₂F₁₂trans, and H₂F₁₈diEster) and two conjugatable porphyrins (H₂F₁₈CO₂H and ZnF₁₈CO₂H). Surface binding was necessary for attaching the porphyrins to the metal-oxide photoanode. Compounds H₂F₁₈diEster, H₂F₁₈Phos, H₂F₁₈Ester, ZnF₁₈Ester, H₂F₁₂cis, and H₂F₁₂trans have protected surface anchoring groups that could be deprotected to generate carboxylic acids and phosphonic acids for binding to metal oxide surfaces.⁴⁷ Zinc metalation of H₂F₁₈Ester and H₂F₁₈CO₂H gave the porphyrins ZnF₁₈Ester and ZnF₁₈CO₂H, respectively. The free-base/metalation pairs (H₂F₁₈Ester and ZnF₁₈Ester) were prepared

for redox potential tuning and IET studies. Porphyrins $H_2F_{12}cis$ and $H_2F_{12}trans$ share the same functional groups and have the same number of trifluoromethylphenyl groups, but different molecular geometries (*cis*- A_2B_2 vs *trans*- A_2B_2) for redox potential tuning purposes. Porphyrins H_2F_{24} and ZnF_{24} , which bear the maximum number of CF_3 groups, are prepared as reference compounds, and the zinc-porphyrin ZnF_{24} can be used for coordination studies with the zinc center.⁴⁸ The *trans*- A_2BC -type porphyrin $H_2F_{18}diEster$ bears two new features when compared with its counterpart molecule, $H_2F_{12}trans$: (1) two additional trifluoromethyl groups were incorporated for further redox potential tuning and (2) a *tert*-butyl ester, instead of methyl ester, facilitates selective hydrolysis to unveil one of the two carboxylic acids for further chemical elaboration.

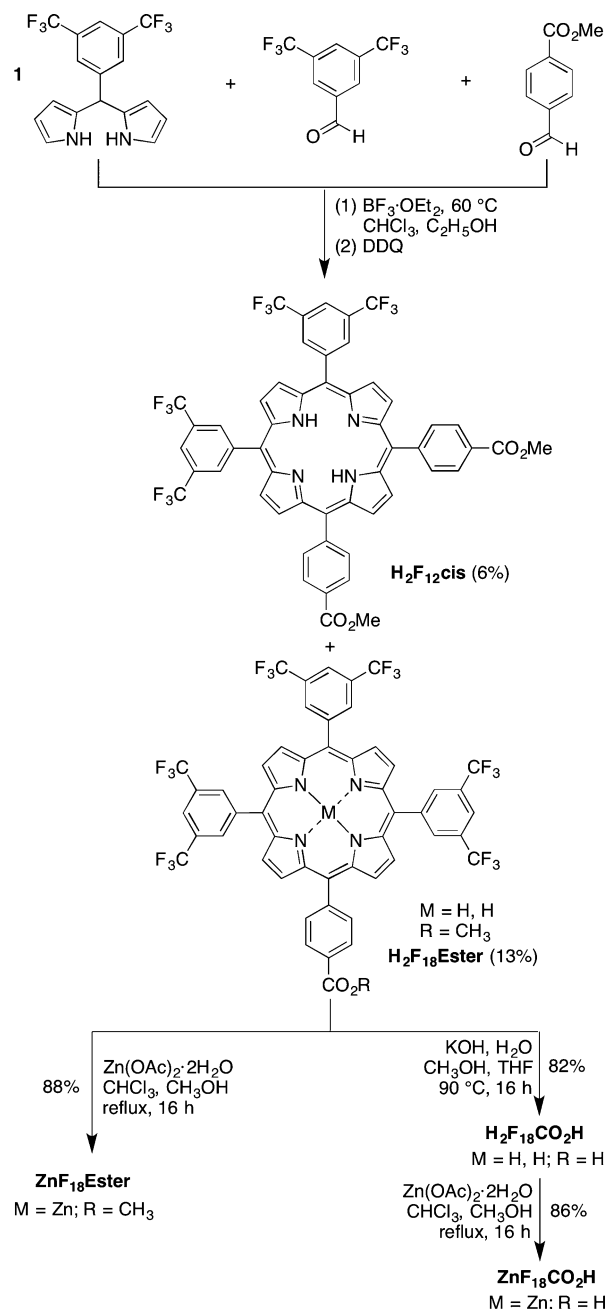
3.2. Synthesis and Characterization. The porphyrins were synthesized by condensation of 5-(3,5-bis-(trifluoromethyl)phenyl)dipyrromethane and the appropriate aldehydes, catalyzed by boron trifluoride-diethyl etherate ($BF_3 \cdot OEt_2$), followed by oxidation with 2,3-dichloro-5,6-dicyanobenzoquinone (DDQ), a procedure developed by Lindsey et al.⁴⁹ Column chromatography afforded each porphyrin in high purity. Following such a standard procedure, porphyrins $H_2F_{18}Ester$ and $H_2F_{12}cis$ were obtained by condensation of 5-(3,5-bis-(trifluoromethyl)phenyl)dipyrromethane **1**, 3,5-bis-(trifluoromethyl) benzaldehyde, and methyl 4-formylbenzoate in 13 and 6% yields, respectively (Scheme 1).⁵⁰ The *cis*- A_2B_2 porphyrin $H_2F_{12}cis$ is a scrambling product in this reaction.⁵¹ Hydrolysis of $H_2F_{18}Ester$ under basic aqueous conditions gave $H_2F_{18}CO_2H$ in 82% yield. Zinc metalation of $H_2F_{12}Ester$ was readily achieved by reaction with zinc acetate dihydrate and the product, $ZnF_{18}Ester$, was easily isolated in 88% yield by column chromatography. Zinc metalation was accompanied by the complete disappearance of the two pyrrolic protons in the 1H NMR spectrum. The same reaction conditions and purification procedures were adopted to prepare porphyrin $ZnF_{18}CO_2H$ in 86% yield.

Preparation of porphyrin $H_2F_{18}diEster$ involved the synthesis of the corresponding benzaldehyde (**4**) bearing two trifluoromethyl groups and a *tert*-butyl ester unit (Scheme 2). Treatment of compound **2** with *tert*-butyl alcohol in the presence of dicyclohexylcarbodiimide (DCC) and 4-dimethylaminopyridine (DMAP) afforded compound **3** in 75% yield. Conversion of phenyl bromide (**3**) to benzaldehyde (**4**) was achieved by treatment of compound **3** with *n*-butyl lithium, followed by addition of DMF. Standard condensation of benzaldehyde **4**, methyl 4-formylbenzoate, and dipyrromethane **1** afforded porphyrin $H_2F_{18}diEster$ in 17% yield.

The preparation of $H_2F_{12}trans$, $H_2F_{18}Phos$, and ZnF_{24} is described in Schemes S1–S3. All porphyrins were characterized by 1H NMR, absorption and emission spectroscopy, and matrix-assisted laser desorption/ionization–mass spectrometry (MALDI-MS).

The regioisomers *trans*- A_2B_2 (porphyrin $H_2F_{12}trans$) and *cis*- A_2B_2 (porphyrin $H_2F_{12}cis$) were distinguished by their unique resonance patterns in the 1H NMR spectra (Figure 1). Porphyrin $H_2F_{12}trans$ has two σ_v symmetry planes, rendering the eight β -protons split into two doublets 8.72 (d, $J = 6.0$ Hz, H3, H7, H13, and H17) and 8.89 (d, $J = 6.0$ Hz, 2H, H2, H8, H12 and H18), while for the case of $H_2F_{12}cis$, there is only one symmetry plane with the eight β -protons split into two doublets and two singlets 8.74 (d, $J = 4.0$ Hz, H8, and H17), 8.77 (s, H12 and H13), 8.86 (s, H2 and H3), and 8.90 (d, $J = 4.0$ Hz, H7 and H8). The protons of the phenyl groups at the

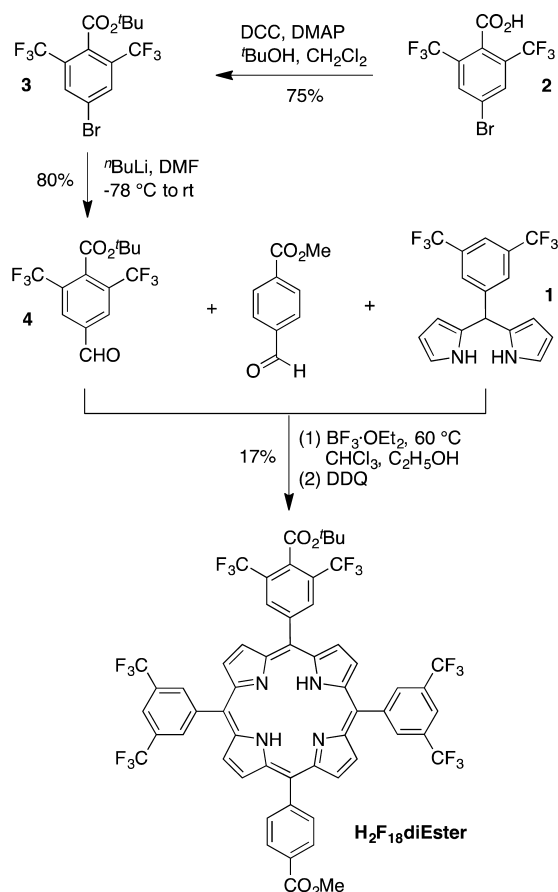
Scheme 1. Synthesis of Zinc Metalated Carboxy-Porphyrins



porphyrin meso positions did not help to distinguish these two porphyrin regioisomers as they gave almost identical chemical shifts and resonance patterns (Figure 1).

3.3. Photophysical and Electrochemical Properties.

The absorption maxima for the Soret and Q-bands as well as the maxima of the fluorescence emission bands are listed in Table 1. All free-base and zinc metalated porphyrins exhibited characteristic porphyrin spectral features, including an intense Soret band, two Q-bands together with two vibronic bands for free-base porphyrins, or one Q-band with one vibronic band for metalloporphyrins. The Soret band represents a transition from the ground-state singlet to a high energy, short-lived singlet state (S_2) which can rapidly interconvert to a lower energy singlet, S_1 . The S_1 state can also be accessed directly from the ground state, corresponding to the Q-band absorbances. Representative absorption and fluorescence spectra of

Scheme 2. Synthesis of Porphyrin H₂F₁₈diEster

H₂F₁₈Ester and ZnF₁₈Ester are presented in Figure 2. The molar extinction coefficients of H₂F₁₈Ester and ZnF₁₈Ester were 373 000 M⁻¹cm⁻¹ at 418 nm and 519 000 M⁻¹cm⁻¹ at 419 nm, respectively, as compared with a value of 407 000 M⁻¹cm⁻¹ for the Soret band of tetraphenylporphyrin in benzene.⁵² These results imply that the electronic structures of the porphyrin core are not significantly perturbed by the CF₃-, carboxy-, or phosphano-phenyl substituents at the porphyrin meso positions. The absorption spectra of the radical cations were also collected (Figure S2), and the peak parameters are listed in Table 1.

The phenyl CF₃ groups affect the electronic structure of the porphyrin ring due to their electron-withdrawing character, which destabilizes the radical cation.^{19,54} As a result, the porphyrins show a highly oxidizing reversible wave in their cyclic voltammograms corresponding to the formation of the radical cation, ranging between 1.25–1.56 V vs NHE, and a second reversible wave, indicative of the dication species, ranging from 1.53–1.76 V vs NHE. Midpoint potentials of the radical cation and dication were obtained using CV and are listed in Table 1. Figure 3 shows cyclic voltammograms of the free-base porphyrins H₂F₁₂trans, H₂F₁₈Ester, and H₂F₂₄ and the Zn-metalated porphyrin ZnF₁₈Ester. Increasing the number of fluorine atoms from 12 to 18 shifted the radical cation potentials in the anodic direction (1.46 V for H₂F₁₂trans vs 1.53 V for H₂F₁₈Ester), while a further increase in the number of fluorine atoms from 18 to 24 did not shift further the radical cation potential (1.53 V for H₂F₁₈Ester vs 1.52 for H₂F₂₄). The zinc-metalated porphyrins have radical cation potentials in the 1.25–1.35 V vs NHE range, significantly lower than those of

the free-base porphyrins which are typically in the 1.46–1.56 V vs NHE range. For example, ZnF₂₄ has potentials cathodically shifted with respect to H₂F₂₄ due to metalation of the porphyrin (1.35 vs 1.52 V). Analogous results have been observed for fluorinated phenyl rings attached to the meso position on porphyrins (Table 1); however, these are prone to nucleophilic aromatic substitution, making them less stable.^{19,54} The phenyl CF₃ groups are not prone to this, representing an improvement in porphyrin design. Each CF₃-porphyrin shows a potential higher than that of its non-CF₃-substituted counterpart, 1.05 V vs NHE for 15-carboxyphenyl-5,10,20-trimesitylporphyrin⁸ and 0.99 V vs NHE for zinc(II)-15-carboxy-5,10,20-trimesitylporphyrin.⁵⁵ Additional cyclic voltammograms of ZnF₂₄, H₂F₁₈Phos, H₂F₁₂cis, and H₂F₁₈diEster are included in Figure S1.

The ground-state potentials for the porphyrin radical cation/porphyrin couple were obtained by CV measurements, while the transition energies were extracted from the intersection of the normalized absorption and fluorescence spectra, which is 1.92 eV for the free-base porphyrins and ~2.10 eV for zinc metalloporphyrins (Figure S3). All of the parameters as well as the conduction band energy levels of two common semiconducting metal oxides TiO₂ and SnO₂, are depicted in Figure 4. The driving force for IET is determined by the energy difference between the excited-state energy of the porphyrin and the conduction band of the semiconductor. The excited-state energies of the two metalloporphyrins ZnF₁₈Ester and ZnF₂₄ lie 0.2–0.3 eV higher than the energy of the conduction band of TiO₂ at pH 6, so these compounds should have enough driving force for IET to TiO₂. All ten porphyrins have excited-state energies 0.3–0.8 V above the SnO₂ conduction band. Therefore, all of the porphyrins should promote IET to SnO₂ as discussed below.

3.4. Quantum Chemistry Calculations. DFT calculations explored the electronic structure of the synthesized fluorinated porphyrins, H₂F₁₈Ester, ZnF₁₈Ester, H₂F₁₈Phos, and H₂F₁₈diEster. Calculated potentials for oxidation Φ_{ox} vs NHE were obtained from the difference in energy between the neutral and oxidized species, respectively, optimized with unrestricted DFT (uDFT) and referred to the potential difference between NHE and vacuum (eq 3):

$$\Phi_{\text{ox}} = E_{\text{ox}} - E_{\text{neutral}} - 4.44 \text{ eV} \quad (3)$$

As shown in Table 2, the calculated potentials are in very good agreement with the CV experiments. ZnF₁₈Ester shows the lowest potential for oxidation vs NHE, correlating with its higher E_{HOMO} compared to that of the other porphyrins. The spin densities of the oxidized doublets show that the hole corresponds to the HOMO orbital, as seen in Figure 5, where the spin densities of the oxidized species and the ground-state frontier orbitals are plotted.

In each of the four computationally studied porphyrins, the two HOMOs and in particular the two LUMOs are respectively near-degenerate, consistent with the Gouterman four-orbital theory.⁵⁶ The energies of these four orbitals are listed in Table 2, which also shows that the four lowest-energy electronic transitions occur between these orbitals, which are responsible for the observed spectral features in the UV–visible region. From Table 2, it is apparent that the three free-base porphyrins show very similar optical properties overall, consistent with the fact that they share the same porphyrin core, where the relevant molecular orbitals are located. The vertical transitions were calculated with linear-response TD-DFT, and the resulting

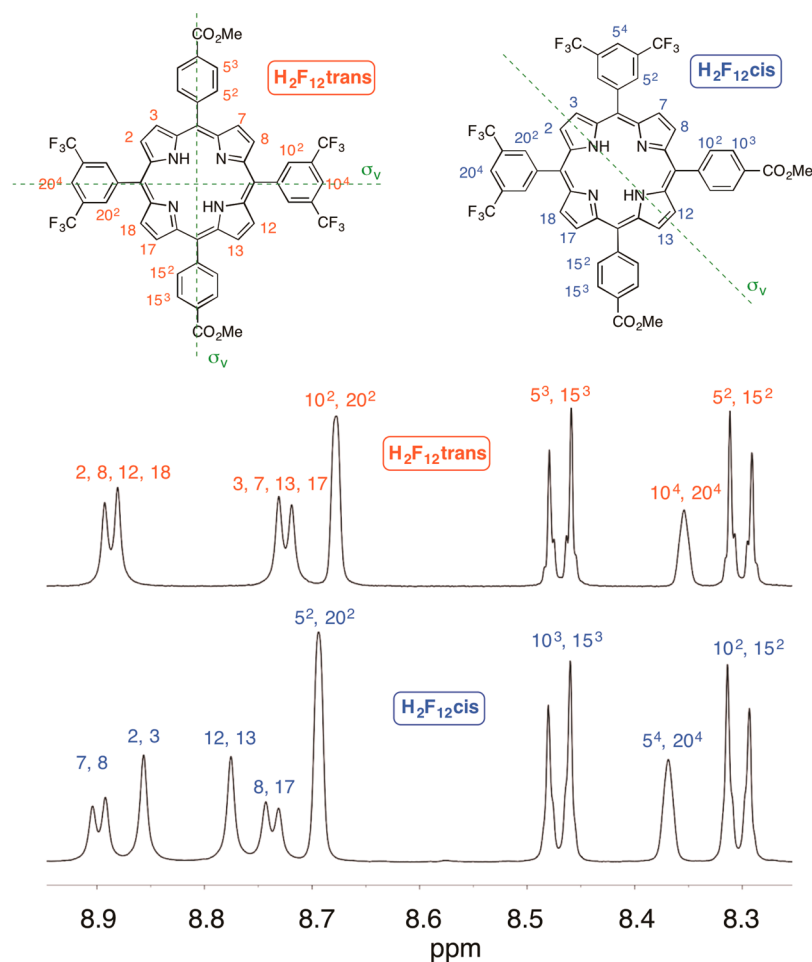


Figure 1. ^1H NMR spectra (aromatic region only) of porphyrins $\text{H}_2\text{F}_{12}\text{trans}$ and $\text{H}_2\text{F}_{12}\text{cis}$ in CDCl_3 .

wavelengths, intensities, and dominant orbital contributions are listed in Table S1. While the experimental spectra show major vibronic splitting of the low energy Q-bands (Figure 2), our calculations did not address vibronic considerations, which partly accounts for the underestimations of calculated absorption wavelengths. The porphyrin core of the Zn-metalated $\text{ZnF}_{18}\text{Ester}$ has an additional symmetry element compared to the free-base porphyrins (D_{4d} vs C_{2v}), causing its Q_x and Q_y bands to collapse to a single experimental absorption peak at 550 nm (545 nm in calculations) with only minor vibronic features.

Experimentally observed Stokes shifts are reproduced in calculations, which are found to arise from small but non-negligible structural relaxation of the S_1 excited state. The energy associated with this relaxation is around 0.04 eV, as seen in Table 2. All four computationally investigated porphyrins have near-planar S_0 ground-state geometries, as shown by the small N–N–N–N dihedral angles (Table 2). The same dihedral angles increase very slightly in the S_1 state, except for $\text{ZnF}_{18}\text{Ester}$, for which the increase of the N–N–N–N dihedral angle in the S_1 state is more substantial, reaching 6.8° . The excited-state twisting is visualized in Figure S4 in the Supporting Information for all four computationally studied porphyrins. Porphyrin $\text{ZnF}_{18}\text{Ester}$ shows the greatest excited-state twisting, correlating with the greatest Stokes shift.

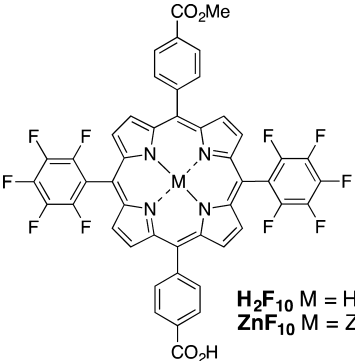
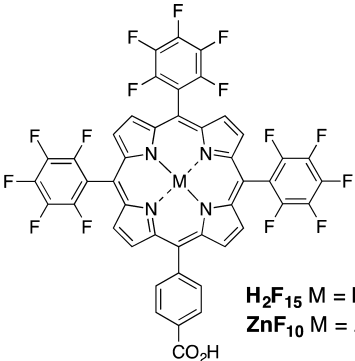
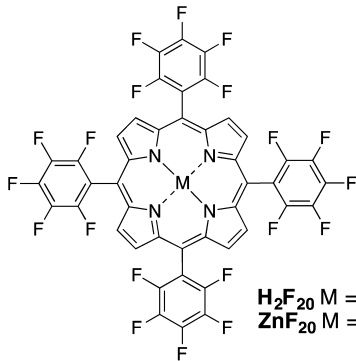
3.5. Electron Injection Measurements. We explored the IET dynamics from $\text{ZnF}_{18}\text{CO}_2\text{H}$ and $\text{H}_2\text{F}_{18}\text{CO}_2\text{H}$ into TiO_2 and SnO_2 surfaces by using TRTS, an ultrafast spectroscopic

technique that can probe transient conductivity in metal oxides with subpicosecond resolution.¹⁸ THz (far-infrared) pulses transmitted through the sample are attenuated by the presence of mobile electrons in the conduction band so that a decrease in transmitted THz amplitude correlates with an increase in carrier density upon electron injection. The increase in conductivity is proportional to the product of the carrier density and mobility; an equivalent carrier density in TiO_2 and SnO_2 will manifest as a smaller change in terahertz amplitude for the TiO_2 sample because of the lower carrier mobility in TiO_2 .⁴⁰

At pH 6, the conduction band of TiO_2 is located at approximately -0.51 V vs NHE (Figure 4).⁵³ For $\text{ZnF}_{18}\text{CO}_2\text{H}$, both the S_1 (-0.85 V vs NHE) and S_2 (estimated at -1.72 V vs NHE¹¹) states lie higher in energy than the TiO_2 conduction band edge, which should facilitate electron transfer into the metal oxide. In contrast, the S_1 state of $\text{H}_2\text{F}_{18}\text{CO}_2\text{H}$ (-0.39 V vs NHE) lies 120 mV below the conduction band edge, making electron injection from the S_1 state into the metal oxide thermodynamically unfavorable, allowing only injection only from the S_2 state (estimated at -1.44 V vs NHE). Though we photoexcite into the S_2 state at 400 nm, the S_2 state in porphyrins is known to rapidly undergo internal conversion into the S_1 state, reducing the efficiency of IET.^{57,58}

Figure 6A shows the TRTS scans for $\text{ZnF}_{18}\text{CO}_2\text{H}$ (red trace) and $\text{H}_2\text{F}_{18}\text{CO}_2\text{H}$ (blue trace) on TiO_2 in 0.1 M Na_2SO_4 (pH 6) as well as on bare TiO_2 films. Both porphyrins exhibit electron injection into the TiO_2 ; however, with $\text{ZnF}_{18}\text{CO}_2\text{H}$ (Figure

Table 1. Electrochemical and Photophysical Properties of High-Potential Porphyrins in Dichloromethane

<div style="display: flex; justify-content: space-around; align-items: flex-end;"> <div style="text-align: center;">  <p>H₂F₁₀ M = H, H ZnF₁₀ M = Zn</p> </div> <div style="text-align: center;">  <p>H₂F₁₅ M = H, H ZnF₁₀ M = Zn</p> </div> <div style="text-align: center;">  <p>H₂F₂₀ M = H, H ZnF₂₀ M = Zn</p> </div> </div>								
porphyrin	no. F ^a	Abs (nm)	Ems (nm)	Φ_f ^b	1 st E _{1/2} ^c (V vs NHE)	2 nd E _{1/2} ^c (V vs NHE)	S ₁ ^d (V vs NHE)	Abs of radical cation (nm) ^e
H ₂ F ₁₂ <i>cis</i>	12	418, 514, 548, 589, 644	648, 709	0.080	1.51	1.75	−0.41	435, 592, 644
H ₂ F ₁₂ <i>trans</i>	12	418, 514, 548, 589, 644	649, 710	0.073	1.46	1.68	−0.46	448, 593, 650
H ₂ F ₁₈ diEster	18	419, 513, 548, 588, 644	648, 710	0.067	1.56	1.76	−0.36	436, 470, 588, 641
H ₂ F ₁₈ Phos	18	418, 513, 547, 588, 644	648, 710	0.068	1.56	1.75	−0.36	435, 468, 589, 640
H ₂ F ₁₈ Ester	18	418, 513, 547, 588, 643	649, 711	0.066	1.53	1.73	−0.39	436, 472, 589, 642
ZnF ₁₈ Ester	18	418, 548	594, 642	0.062	1.25	1.53	−0.85	435, 589, 640
H ₂ F ₂₄	24	417, 513, 546, 588, 643	648, 710	0.061	1.52	1.70	−0.4	433, 586, 636
ZnF ₂₄	24	419, 547	596, 640	0.057	1.35	1.58	−0.76	432, 588, 637
H ₂ F ₁₀ ^f	10				1.57	1.78	−0.36	
ZnF ₁₀ ^f	10				1.35	1.59	−0.77	
H ₂ F ₁₅ ^g	15	413, 507, 536, 583, 637	641, 706		1.68	1.93		
ZnF ₁₅ ^{g,h}	15	415, 544, 578	585, 637		1.47	1.72	−0.66	
H ₂ F ₂₀	20				1.73	1.98		
ZnF ₂₀ ⁱ	20				1.56		−0.57	

^aThe total number of fluorine atoms on each porphyrin. ^bDetermined in CH₂Cl₂ relative to that of tetramesitylporphyrin in toluene (Φ_f = 0.088) with correction for refractive index differences. ^cOxidative midpoint potentials. ^dExcited-state potentials. ^eDetermined in 0.1 M TBAPF₆ in CH₂Cl₂. ^fData from reference 19. ^gData from reference 11. ^hData from reference 33. ⁱData from reference 53.

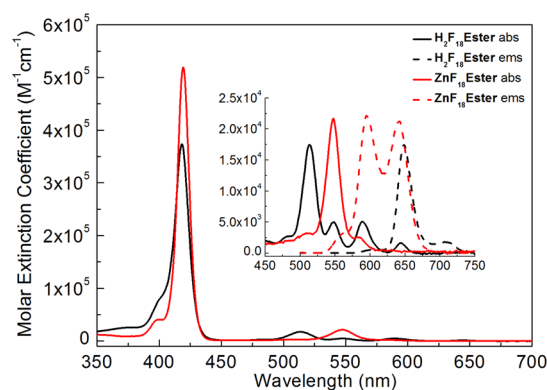


Figure 2. Absorption and fluorescence spectra of H₂F₁₈Ester and ZnF₁₈Ester in dichloromethane. The fluorescence spectra are normalized according to the intensity of their most intense absorption Q-bands.

6B), we observe a significantly higher injection amplitude as manifested by a larger decrease in THz amplitude. This is consistent with the increased driving force for injection by ZnF₁₈CO₂H as well as the ability to inject from both the S₂ and S₁ states, while H₂F₁₈CO₂H may only inject from the S₂ state. To characterize the injection kinetics of ZnF₁₈CO₂H and H₂F₁₈CO₂H, we fit eq 2 to the measured traces (Table 3).

For ZnF₁₈CO₂H, the injection is best described by three components with an additional fourth component describing electron trapping. For H₂F₁₈CO₂H, the injection is best

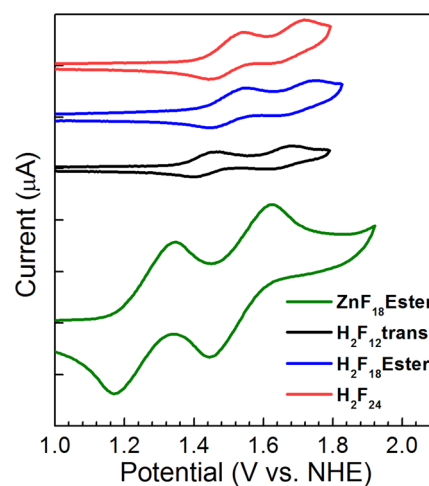


Figure 3. Cyclic voltammograms of H₂F₂₄, H₂F₁₈Ester, H₂F₁₂*trans*, and ZnF₁₈Ester in 0.1 M TBAPF₆ in dichloromethane with a 50 mV/s scan rate.

described by two components with a third trapping component. In both samples, there is a fast component, instrument response limited in the case of ZnF₁₈CO₂H, which likely corresponds to injection from S₂. For ZnF₁₈CO₂H, there is also a slightly slower 5 ps component, which may correspond to injection from S₁. Finally, both porphyrins exhibit a long-time component (71 ps for ZnF₁₈CO₂H and 221 ps for H₂F₁₈CO₂H) that cannot be readily explained as injection

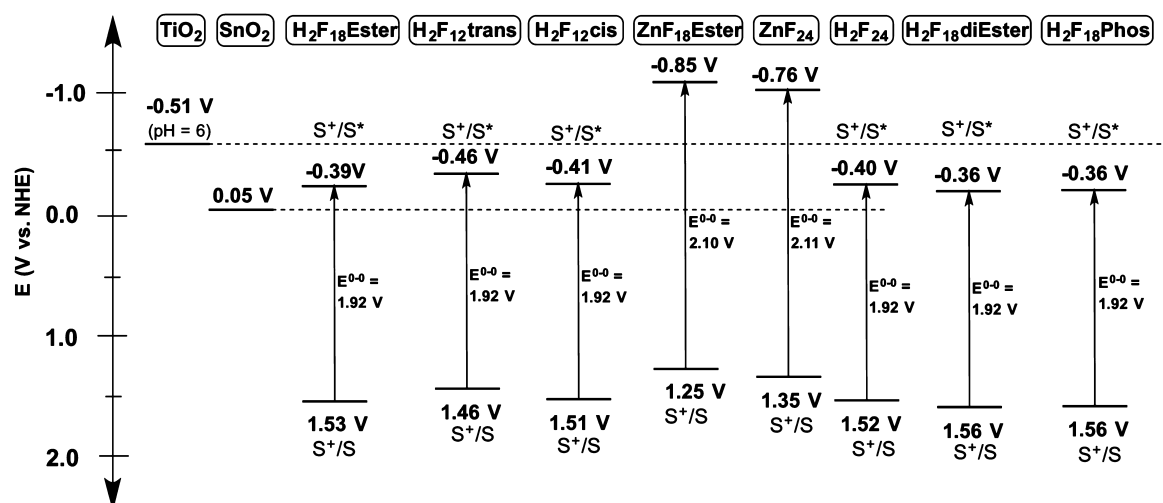


Figure 4. Energy level diagram illustrating the ground and excited-state (S_1) potentials.

Table 2. DFT Results^a

	H ₂ F ₁₈ diEster	H ₂ F ₁₈ Phos	H ₂ F ₁₈ Ester	ZnF ₁₈ Ester
$E_{\text{HOMO}-1}$ (eV)	-6.27	-6.26	-6.26	-6.10
E_{HOMO} (eV)	-6.01	-6.01	-5.99	-5.92
E_{LUMO} (eV)	-3.07	-3.06	-3.06	-2.90
$E_{\text{LUMO}+1}$ (eV)	-3.06	-3.04	-3.05	-2.89
$\Phi_{\text{ox},1}$ (eV)	1.34	1.33	1.32	1.23
S_0 N–N–N–N angle (°)	1.07	1.04	1.04	2.12
S_1 N–N–N–N angle (°)	1.76	1.54	1.52	6.83
λ_1 (nm)	589.7	588.9	591.1	545.4
S_1 relaxation (eV)	0.041	0.039	0.039	0.043
emission λ_1 (nm)	604.6	603.3	606.2	570.4
Stokes shift (nm/eV)	14.9/0.052	14.3/0.050	15.2/0.049	20.7/0.083

^aGround-state frontier orbital energies vs vacuum, potentials for oxidation, and N–N–N–N dihedral angles. Optimized S_1 excited-state N–N–N–N dihedrals, structural relaxation energies, and emission wavelengths at the S_1 geometry.

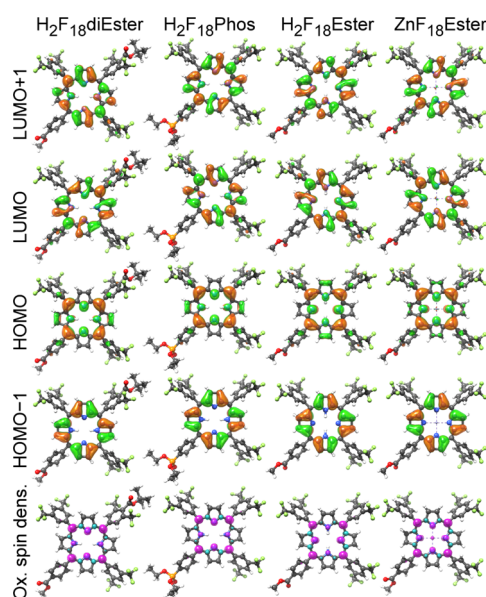


Figure 5. Four frontier orbitals and the oxidized state spin density of H₂F₁₈diEster, H₂F₁₈Phos, H₂F₁₈Ester, and ZnF₁₈Ester.

from the S_2 or S_1 states. We suggest that this component is related to electrons that were injected into nonmobile surface

states and undergo slower thermal relaxation into the conduction band.⁴⁰

We also explored injection of both ZnF₁₈CO₂H and H₂F₁₈CO₂H into SnO₂ at pH 6. The conduction band of SnO₂ is roughly 0.5 V lower than that of TiO₂, which allows for a higher injection yield⁴⁰ and, in the case of H₂F₁₈CO₂H, allows for injection from both the S_2 and S_1 states. Figure 6B shows the TRTS scans for ZnF₁₈CO₂H (red trace) and H₂F₁₈CO₂H (blue trace) on SnO₂. Both show similar injection amplitudes; however, injection from H₂F₁₈CO₂H is noticeably slower as a result of the lower driving force for injection. The injection kinetics for both porphyrins can be described by three components with no evidence of trapping. Both exhibit an ultrafast component (Table 3) that likely corresponds to injection from the S_2 state but comprises a fraction of the overall injection smaller than that on TiO₂. The second component, likely injection from S_1 , is also slower for both porphyrins. It is generally observed that injection into SnO₂ is slower than injection into TiO₂ because of the lower density of states in the conduction band of SnO₂.^{59,60} The origin of the third component may correspond to injection from the triplet state or, as with TiO₂, be related to electrons thermally relaxing from nonmobile surface states.

The observed dynamics of IET from ZnF₁₈CO₂H and H₂F₁₈CO₂H are generally in agreement with other TRTS studies of high potential porphyrins. Milot et al. observed

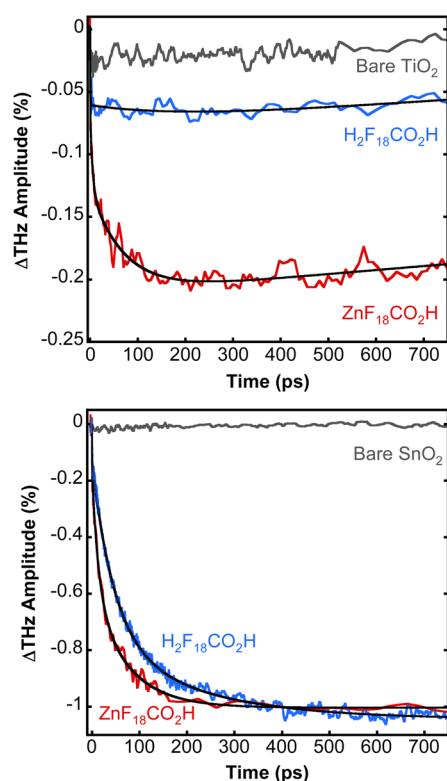


Figure 6. TRTS scans of $\text{ZnF}_{18}\text{CO}_2\text{H}$ (red) and $\text{H}_2\text{F}_{18}\text{CO}_2\text{H}$ (blue) on TiO_2 (top) and SnO_2 (bottom) as well as bare TiO_2 and SnO_2 (gray) in 0.1 M Na_2SO_4 (pH 6). Solid black lines are fits of eq 2.

roughly the same ratio of injection amplitudes for zinc(II)-15-carboxyphenyl-5,10,20-tris(pentafluorophenyl)porphyrin (ZnF_{15}) and 15-carboxyphenyl-5,10,20-tris(pentafluorophenyl)porphyrin (H_2F_{15}) on TiO_2 as those that we observe for $\text{ZnF}_{18}\text{CO}_2\text{H}$ and $\text{H}_2\text{F}_{18}\text{CO}_2\text{H}$, though the injection kinetics were significantly faster because those samples were measured in air rather than in an aqueous solution.¹¹ On SnO_2 , they also observed roughly the same injection amplitude for ZnF_{15} and H_2F_{15} with the injection kinetics for H_2F_{15} slower than that for ZnF_{15} . Moore et al. found identical trends when examining zinc and free-base 5-(4-carbomethoxyphenyl)-15-(4-carboxyphenyl)-10,20-bis(pentafluorophenyl)porphyrin (H_2F_{10}) porphyrins.¹⁹

3.6. Electron Recombination Measurements. We explored the recombination kinetics of $\text{ZnF}_{18}\text{CO}_2\text{H}$ and $\text{H}_2\text{F}_{18}\text{CO}_2\text{H}$ on SnO_2 at pH 6 (Figure 7). The transient spectra for $\text{ZnF}_{18}\text{CO}_2\text{H}$ on SnO_2 show a large bleach of the Soret band between 400 and 450 nm, a new feature between 450 and 500 nm, and a bleach of the Q-band centered at 560 nm. There is also a small transient absorbance at wavelengths longer than 580 nm. We assign the feature between 450 and 500 nm to the formation and loss of the porphyrin radical

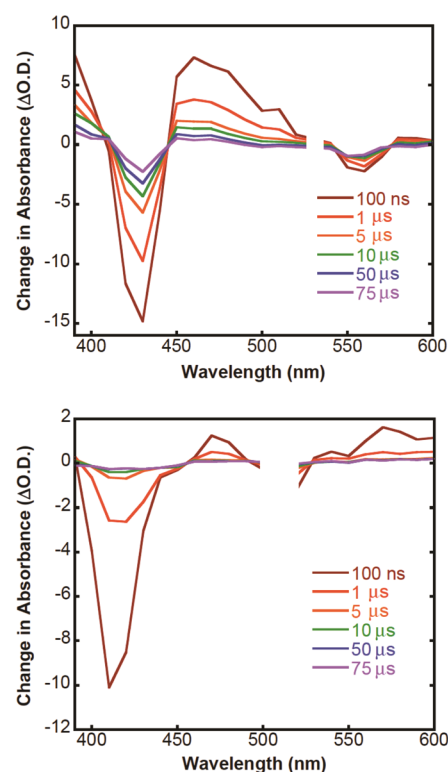


Figure 7. Transient spectra of $\text{ZnF}_{18}\text{CO}_2\text{H}$ (top) and $\text{H}_2\text{F}_{18}\text{CO}_2\text{H}$ (bottom) on SnO_2 at pH 6. $\text{ZnF}_{18}\text{CO}_2\text{H}$ and $\text{H}_2\text{F}_{18}\text{CO}_2\text{H}$ were excited with 5 mJ pulses (7 ns, 10 mm diameter) at 530 and 505 nm, respectively.

cation^{61,62} following injection into SnO_2 . This transient absorbance decays with a $t_{1/2} \sim 2 \mu\text{s}$, which is consistent with the results that Nayak et al. reported with a high-potential, fluorinated zinc porphyrin on SnO_2 .⁶²

For $\text{H}_2\text{F}_{18}\text{CO}_2\text{H}$, we see a similar bleach of the Soret band, a transient absorption near 470 nm, a bleach between 490 and 520 nm, and a broad transient absorbance at wavelengths longer than 520 nm. Similarly, these features are also assigned to the formation of the porphyrin radical cation after injection into SnO_2 .^{62,63} Surprisingly, the decay of the radical cation feature is significantly more rapid than with $\text{ZnF}_{18}\text{CO}_2\text{H}$. Recombination of injected electrons with the oxidized porphyrin is nearly complete within 1 μs . The ground state for $\text{H}_2\text{F}_{18}\text{CO}_2\text{H}$ is nearly 300 mV more positive than the ground state of $\text{ZnF}_{18}\text{CO}_2\text{H}$, introducing significantly more driving force for recombination as demonstrated by the rapid disappearance of the radical cation.

4. CONCLUSIONS

We successfully designed, synthesized, and characterized a promising set of new trifluoromethylated porphyrins that provide valuable physical insights into the mechanisms of IET.

Table 3. Fit Parameters for $\text{H}_2\text{F}_{18}\text{CO}_2\text{H}$ and $\text{ZnF}_{18}\text{CO}_2\text{H}$ on TiO_2 and SnO_2 in 0.1 M Na_2SO_4 (pH 6)^a

metal oxide	porphyrin	A_1	τ_1 (ps)	A_2	τ_2 (ps)	A_3	τ_3 (ps)	A_4	τ_4 (ps)	scaling factor
TiO_2	$\text{H}_2\text{F}_{18}\text{CO}_2\text{H}$	0.74	0.6	0.26	221			−0.96	1989	0.083
	$\text{ZnF}_{18}\text{CO}_2\text{H}$	0.34	<0.5	0.26	5	0.40	71	−1.00	5956	0.215
SnO_2	$\text{H}_2\text{F}_{18}\text{CO}_2\text{H}$	0.12	<0.5	0.59	47	0.29	207			1.03
	$\text{ZnF}_{18}\text{CO}_2\text{H}$	0.17	<0.5	0.41	14	0.42	73			0.99

^aData from Figure 6 fit using eq 2.

The redox potentials were tuned by modifying the substituents on the porphyrin meso positions and by interconverting between the free-base and metalated species. Electrochemical studies showed that the reported porphyrins display sufficiently high ground-state potentials to permit water oxidation as well as excited-state potentials suitable for IET. DFT calculations highlight the correlation between deep frontier molecular orbitals and high potentials and provide insights into the geometric and electronic structure, e.g., with respect to Stokes shifts. Our TRTS results show that both metalated and free-base porphyrins have comparable electron injection kinetics on SnO_2 and that zinc metalloporphyrins inject more efficiently on TiO_2 than the free-base porphyrin. Transient absorption spectroscopy on SnO_2 confirm electron injection from both free-base and metalated porphyrins; however, recombination is significantly more rapid in the case of the free-base porphyrin, likely as a result of the greater driving force for recombination. The successful preparation of these newly designed porphyrins and promising spectroscopic results encourage applications of these compounds for use in photocatalytic solar cells. Further studies, including structural modifications for better electrochemical and photophysical properties and use in water-splitting dye-sensitized photoelectrochemical cells, are currently underway.

■ ASSOCIATED CONTENT

■ Supporting Information

This information can be found online for free at The Supporting Information is available free of charge on the ACS Publications website at DOI: 10.1021/acs.jpcc.6b10350.

Synthesis and characterization of porphyrins, CV data, transition energy measurements, and details on calculated electronic transitions (PDF)

■ AUTHOR INFORMATION

Corresponding Authors

*Phone: 203-200-8936; E-mail: robert.crabtree@yale.edu.

*Phone: 203-432-5049; E-mail: charles.schmittenmaer@yale.edu.

*Phone: 203-432-6672; E-mail: victor.batista@yale.edu.

*Phone: 203-432-5202; E-mail: gary.brudvig@yale.edu.

ORCID

Gary W. Brudvig: 0000-0002-7040-1892

Notes

The authors declare no competing financial interest.

■ ACKNOWLEDGMENTS

This work was supported by the U.S. Department of Energy, Chemical Sciences, Geosciences, and Biosciences Division, Office of Basic Energy Sciences, Office of Science (Grant DE-FG02-07ER15909). Additional support was provided by a generous donation from the TomKat Charitable Trust. We thank Terence Wu and Mousumi Ghosh in the Yale West Campus Analytical Core for help with NMR and MALDI-MS measurements. V.S.B. acknowledges support from the Argonne-Northwestern Solar Energy Research (ANSER) Center, an Energy Frontier Research Center funded by the U.S. Department of Energy, Office of Science, Office of Basic Energy Sciences (US DOE-OS-BES) under Award DE-SC0001059. Computational work was supported by the Center

for High Performance Computing, Shanghai Jiao Tong University, and the Yale Center for Research Computing.

■ REFERENCES

- (1) Badawy, W. A. A Review on Solar Cells from Si-Single Crystals to Porous Materials and Quantum Dots. *J. Adv. Res.* **2015**, *6*, 123–132.
- (2) Ragoussi, M. E.; Torres, T. New Generation Solar Cells: Concepts, Trends and Perspectives. *Chem. Commun.* **2015**, *51*, 3957–3972.
- (3) Sum, T. C.; Mathews, N. Advancements in Perovskite Solar Cells: Photophysics Behind the Photovoltaics. *Energy Environ. Sci.* **2014**, *7*, 2518–2534.
- (4) Swierk, J. R.; Mallouk, T. E. Design and Development of Photoanodes for Water-Splitting Dye-Sensitized Photoelectrochemical Cells. *Chem. Soc. Rev.* **2013**, *42*, 2357–2387.
- (5) Gao, Y.; Ding, X.; Liu, J.; Wang, L.; Lu, Z.; Li, L.; Sun, L. Visible Light Driven Water Splitting in a Molecular Device with Unprecedentedly High Photocurrent Density. *J. Am. Chem. Soc.* **2013**, *135*, 4219–4222.
- (6) Zhao, Y.; Swierk, J. R.; Megiatto, J. D., Jr.; Sherman, B.; Youngblood, W. J.; Qin, D.; Lentz, D. M.; Moore, A. L.; Moore, T. A.; Gust, D.; et al. Improving the Efficiency of Water Splitting in Dye-Sensitized Solar Cells by Using a Biomimetic Electron Transfer Mediator. *Proc. Natl. Acad. Sci. U. S. A.* **2012**, *109*, 15612–15616.
- (7) Hanson, K.; Brennaman, M. K.; Ito, A.; Luo, H.; Song, W.; Parker, K. A.; Ghosh, R.; Norris, M. R.; Glasson, C. R. K.; Concepcion, J. J.; et al. Structure–Property Relationships in Phosphonate-Derivatized, Ru^{II} Polypyridyl Dyes on Metal Oxide Surfaces in an Aqueous Environment. *J. Phys. Chem. C* **2012**, *116*, 14837–14847.
- (8) Swierk, J. R.; Mendez-Hernandez, D. D.; McCool, N. S.; Liddell, P.; Terazono, Y.; Pahk, I.; Tomlin, J. J.; Oster, N. V.; Moore, T. A.; Moore, A. L.; et al. Metal-Free Organic Sensitizers for Use in Water-Splitting Dye-Sensitized Photoelectrochemical Cells. *Proc. Natl. Acad. Sci. U. S. A.* **2015**, *112*, 1681–1686.
- (9) Poddutoori, P. K.; Thomsen, J. M.; Milot, R. L.; Sheehan, S. W.; Negre, C. F. A.; Garapati, V. K. R.; Schmittenmaer, C. A.; Batista, V. S.; Brudvig, G. W.; van der Est, A. Interfacial Electron Transfer in Photoanodes Based on Phosphorus(V) Porphyrin Sensitizers Codeposited on SnO_2 with the $\text{Ir}^{\text{III}}\text{Cp}^*$ Water Oxidation Precatalyst. *J. Mater. Chem. A* **2015**, *3*, 3868–3879.
- (10) Moore, G. F.; Blakemore, J. D.; Milot, R. L.; Hull, J. F.; Song, H.-e.; Cai, L.; Schmittenmaer, C. A.; Crabtree, R. H.; Brudvig, G. W. A Visible Light Water-Splitting Cell with a Photoanode Formed by Codeposition of a High-Potential Porphyrin and an Iridium Water-Oxidation Catalyst. *Energy Environ. Sci.* **2011**, *4*, 2389–2392.
- (11) Milot, R. L.; Moore, G. F.; Crabtree, R. H.; Brudvig, G. W.; Schmittenmaer, C. A. Electron Injection Dynamics from Photoexcited Porphyrin Dyes into SnO_2 and TiO_2 Nanoparticles. *J. Phys. Chem. C* **2013**, *117*, 21662–21670.
- (12) Vagnini, M. T.; Smeigh, A. L.; Blakemore, J. D.; Eaton, S. W.; Schley, N. D.; D'Souza, F.; Crabtree, R. H.; Brudvig, G. W.; Co, D. T.; Wasielewski, M. R. Ultrafast Photodriver Intramolecular Electron Transfer from an Iridium-Based Water-Oxidation Catalyst to Perylene Diimide Derivatives. *Proc. Natl. Acad. Sci. U. S. A.* **2012**, *109*, 15651–15656.
- (13) Li, F.; Fan, K.; Xu, B.; Gabrielson, E.; Daniel, Q.; Li, L.; Sun, L. Organic Dye-Sensitized Tandem Photoelectrochemical Cell for Light Driven Total Water Splitting. *J. Am. Chem. Soc.* **2015**, *137*, 9153–9159.
- (14) Ronconi, F.; Syrgiannis, Z.; Bonasera, A.; Prato, M.; Argazzi, R.; Caramori, S.; Cristino, V.; Bignozzi, C. A. Modification of Nanocrystalline WO_3 with a Dicationic Perylene Bisimide: Applications to Molecular Level Solar Water Splitting. *J. Am. Chem. Soc.* **2015**, *137*, 4630–4633.
- (15) Vougioukalakis, G. C.; Philippopoulos, A. I.; Stergiopoulos, T.; Falaras, P. Contributions to the Development of Ruthenium-Based Sensitizers for Dye-Sensitized Solar Cells. *Coord. Chem. Rev.* **2011**, *255*, 2602–2621.

- (16) Higashino, T.; Imahori, H. Porphyrins as Excellent Dyes for Dye-Sensitized Solar Cells: Recent Developments and Insights. *Dalton Trans.* **2015**, *44*, 448–463.
- (17) Lapides, A. M.; Sherman, B. D.; Brennaman, M. K.; Dares, C. J.; Skinner, K. R.; Templeton, J. L.; Meyer, T. J. Synthesis, Characterization, and Water Oxidation by a Molecular Chromophore-Catalyst Assembly Prepared by Atomic Layer Deposition. The “Mummy” Strategy. *Chem. Sci.* **2015**, *6*, 6398–6406.
- (18) Milot, R. L.; Schmittenmaer, C. A. Electron Injection Dynamics in High-Potential Porphyrin Photoanodes. *Acc. Chem. Res.* **2015**, *48*, 1423–1431.
- (19) Moore, G. F.; Konezny, S. J.; Song, H.-e.; Milot, R. L.; Blakemore, J. D.; Lee, M. L.; Batista, V. S.; Schmittenmaer, C. A.; Crabtree, R. H.; Brudvig, G. W. Bioinspired High-Potential Porphyrin Photoanodes. *J. Phys. Chem. C* **2012**, *116*, 4892–4902.
- (20) Leroy, J.; Bondon, A. β -Fluorinated Porphyrins and Related Compounds: An Overview. *Eur. J. Org. Chem.* **2008**, *2008*, 417–433.
- (21) Antoniuk-Pablant, A.; Terazono, Y.; Brennan, B. J.; Sherman, B. D.; Megiatto, J. D., Jr.; Brudvig, G. W.; Moore, A. L.; Moore, T. A.; Gust, D. A New Method for the Synthesis of β -Cyano Substituted Porphyrins and Their Use as Sensitizers in Photoelectrochemical Devices. *J. Mater. Chem. A* **2016**, *4*, 2976–2985.
- (22) Ozette, K.; Battioni, P.; Leduc, P.; Bartoli, J.-F.; Mansuy, D. A New Manganese- β -Heptanitro-Porphyrin with Extreme Redox Potentials: Spectral, Electrochemical and Catalytic Properties. *Inorg. Chim. Acta* **1998**, *272*, 4–6.
- (23) Andou, Y.; Shiragami, T.; Shima, K.; Yasuda, M. Synthesis and Fluorescence Study of a (2-Naphthoxy)Polyoxalkoxyantimony(V) Tetraphenylporphyrin Complex. *J. Photochem. Photobiol., A* **2002**, *147*, 191–197.
- (24) Shiragami, T.; Matsumoto, J.; Inoue, H.; Yasuda, M. Antimony Porphyrin Complexes as Visible-Light Driven Photocatalyst. *J. Photochem. Photobiol., C* **2005**, *6*, 227–248.
- (25) Golf, H. R.; Reissig, H. U.; Wiehe, A. Nucleophilic Substitution on (Pentafluorophenyl)Dipyrromethane: A New Route to Building Blocks for Functionalized Bodipys and Tetrapyrroles. *Org. Lett.* **2015**, *17*, 982–985.
- (26) Hyland, M. A.; Morton, M. D.; Bruckner, C. Meso-Tetrakis(Pentafluorophenyl)Porphyrin-Derived Chromene-Annulated Chlorins. *J. Org. Chem.* **2012**, *77*, 3038–3048.
- (27) Velasco, V. M.; Zolotukhin, M. G.; Guzmán-Gutiérrez, M. T.; Morales, S. L.; Fomine, S.; Carreón-Castro, M. P.; Salmón, M.; Scherf, U. Novel Aromatic Polymers with Pentafluorophenyl Pendent Groups. *Macromolecules* **2008**, *41*, 8504–8512.
- (28) Golf, H. R.; Reissig, H. U.; Wiehe, A. Synthesis of SF₅-Substituted Tetrapyrroles, Metalloporphyrins, BODIPYs, and Their Dipyrane Precursors. *J. Org. Chem.* **2015**, *80*, 5133–5143.
- (29) Shabalin, A. Y.; Adonin, N. Y.; Bardin, V. V.; Prihod'ko, S. A.; Timofeeva, M. N.; Bykova, M. V.; Parmon, V. N. Synthesis of K[4-ROCF₂BF₃] from Potassium Pentafluorophenyltrifluoroborate and O-Nucleophiles. *J. Fluorine Chem.* **2013**, *149*, 82–87.
- (30) Suzuki, M.; Shimizu, S.; Shin, J.-Y.; Osuka, A. Regioselective Nucleophilic Substitution Reaction of Meso-Hexakis-(Pentafluorophenyl) Substituted [26]Hexaphyrin. *Tetrahedron Lett.* **2003**, *44*, 4597–4601.
- (31) Bhupathiraju, N. V. S. D. K.; Rizvi, W.; Batteas, J. D.; Drain, C. M. Fluorinated Porphyrinoids as Efficient Platforms for New Photonic Materials, Sensors, and Therapeutics. *Org. Biomol. Chem.* **2016**, *14*, 389–408.
- (32) Rehm, D.; Weller, A. Kinetics and Mechanics of Electron Transfer During Fluorescence Quenching in Acetonitrile. *Ber. Bunsenges.* **1969**, *73*, 834–839.
- (33) Sawyer, D. T.; Sobkowiak, A.; Roberts, J. L. *Electrochemistry for Chemists*, 2nd ed.; Wiley: New York, 1995.
- (34) R. D., Frisch, M. J.; Trucks, G. W.; Schlegel, H. B.; Scuseria, G. E.; Robb, M. A.; Cheeseman, J. R.; Scalmani, G.; Barone, V.; Mennucci, B.; Petersson, G. A.; et al. *Gaussian09*, revision D.01; Gaussian, Inc.: Wallingford, CT, 2009.
- (35) Cancès, E.; Mennucci, B.; Tomasi, J. A New Integral Equation Formalism for the Polarizable Continuum Model: Theoretical Background and Applications to Isotropic and Anisotropic Dielectrics. *J. Chem. Phys.* **1997**, *107*, 3032–3041.
- (36) Adamo, C.; Barone, V. Toward Reliable Density Functional Methods without Adjustable Parameters: The PBE0 Model. *J. Chem. Phys.* **1999**, *110*, 6158–6170.
- (37) Cai, Z. L.; Crossley, M. J.; Reimers, J. R.; Kobayashi, R.; Amos, R. D. Density Functional Theory for Charge Transfer: The Nature of the N-Bands of Porphyrins and Chlorophylls Revealed through CAM-B3LYP, CASPT2, and SAC-CI Calculations. *J. Phys. Chem. B* **2006**, *110*, 15624–15632.
- (38) Reimers, J. R.; Cai, Z. L.; Kobayashi, R.; Ratsep, M.; Freiberg, A.; Krausz, E. Assignment of the Q-Bands of the Chlorophylls: Coherence Loss Via Q_x - Q_y Mixing. *Sci. Rep.* **2013**, *3*, 2761.
- (39) Nemes, C. T.; Koenigsmann, C.; Schmittenmaer, C. A. Functioning Photoelectrochemical Devices Studied with Time-Resolved Terahertz Spectroscopy. *J. Phys. Chem. Lett.* **2015**, *6*, 3257–3262.
- (40) Swierk, J. R.; McCool, N. S.; Nemes, C. T.; Mallouk, T. E.; Schmittenmaer, C. A. Ultrafast Electron Injection Dynamics of Photoanodes for Water-Splitting Dye-Sensitized Photoelectrochemical Cells. *J. Phys. Chem. C* **2016**, *120*, 5940–5948.
- (41) Turner, G. M.; Beard, M. C.; Schmittenmaer, C. A. Carrier Localization and Cooling in Dye-Sensitized Nanocrystalline Titanium Dioxide. *J. Phys. Chem. B* **2002**, *106*, 11716–11719.
- (42) Beard, M. C.; Turner, G. M.; Schmittenmaer, C. A. Transient Photoconductivity in Gaas as Measured by Time-Resolved Terahertz Spectroscopy. *Phys. Rev. B: Condens. Matter Mater. Phys.* **2000**, *62*, 15764–15777.
- (43) Baxter, J. B.; Schmittenmaer, C. A. Conductivity of ZnO Nanowires, Nanoparticles, and Thin Films Using Time-Resolved Terahertz Spectroscopy. *J. Phys. Chem. B* **2006**, *110*, 25229–25239.
- (44) Cook, D. J.; Hochstrasser, R. M. Intense Terahertz Pulses by Four-Wave Rectification in Air. *Opt. Lett.* **2000**, *25*, 1210–1212.
- (45) Bartel, T.; Gaal, P.; Reimann, K.; Woerner, M.; Elsaesser, T. Generation of Single-Cycle THz Transients with High Electric-Field Amplitudes. *Opt. Lett.* **2005**, *30*, 2805–2807.
- (46) Wu, Q.; Zhang, X. C. Free-Space Electro-Optic Sampling of Terahertz Beams. *Appl. Phys. Lett.* **1995**, *67*, 3523–3525.
- (47) Brennan, B. J.; Llansola Portoles, M. J.; Liddell, P. A.; Moore, T. A.; Moore, A. L.; Gust, D. Comparison of Silatrane, Phosphonic Acid, and Carboxylic Acid Functional Groups for Attachment of Porphyrin Sensitizers to TiO₂ in Photoelectrochemical Cells. *Phys. Chem. Chem. Phys.* **2013**, *15*, 16605–16614.
- (48) Negre, C. F. A.; Milot, R. L.; Martini, L. A.; Ding, W.; Crabtree, R. H.; Schmittenmaer, C. A.; Batista, V. S. Efficiency of Interfacial Electron Transfer from Zn-Porphyrin Dyes into TiO₂ Correlated to the Linker Single Molecule Conductance. *J. Phys. Chem. C* **2013**, *117*, 24462–24470.
- (49) Lindsey, J. S.; Schreiman, I. C.; Hsu, H. C.; Kearney, P. C.; Marguerettaz, A. M. Rothmund and Adler-Longo Reactions Revisited: Synthesis of Tetraphenylporphyrins under Equilibrium Conditions. *J. Org. Chem.* **1987**, *52*, 827–836.
- (50) Gryko, D. T.; Clausen, C.; Lindsey, J. S. Thiol-Derivatized Porphyrins for Attachment to Electroactive Surfaces. *J. Org. Chem.* **1999**, *64*, 8635–8647.
- (51) Geier III, G. R.; Littler, B. J.; Lindsey, J. S. Investigation of Porphyrin-Forming Reactions. Part 3. The Origin of Scrambling in Dipyrromethane+Aldehyde Condensations Yielding *trans*-A₂B₂-Tetraarylporphyrins. *J. Chem. Soc., Perkin Trans. 2* **2001**, 701–711.
- (52) Fonda, H. N.; Gilbert, J. V.; Cormier, R. A.; Sprague, J. R.; Kamioka, K.; Connolly, J. S. Spectroscopic, Photophysical, and Redox Properties of Some Meso-Substituted Free-Base Porphyrins. *J. Phys. Chem.* **1993**, *97*, 7024–7033.
- (53) Martini, L. A.; Moore, G. F.; Milot, R. L.; Cai, L. Z.; Sheehan, S. W.; Schmittenmaer, C. A.; Brudvig, G. W.; Crabtree, R. H. Modular Assembly of High-Potential Zinc Porphyrin Photosensitizers Attached

to TiO₂ with a Series of Anchoring Groups. *J. Phys. Chem. C* **2013**, *117*, 14526–14533.

(54) Moore, G. F.; Hambourger, M.; Gervaldo, M.; Poluektov, O. G.; Rajh, T.; Gust, D.; Moore, T. A.; Moore, A. L. A Bioinspired Construct That Mimics the Proton Coupled Electron Transfer between P680^{•+} and the Tyr(Z)-His190 Pair of Photosystem II. *J. Am. Chem. Soc.* **2008**, *130*, 10466–10467.

(55) Imahori, H.; Hayashi, S.; Hayashi, H.; Oguro, A.; Eu, S.; Umeyama, T.; Matano, Y. Effects of Porphyrin Substituents and Adsorption Conditions on Photovoltaic Properties of Porphyrin-Sensitized TiO₂ Cells. *J. Phys. Chem. C* **2009**, *113*, 18406–18413.

(56) Gouterman, M.; Wagnière, G. H.; Snyder, L. C. Spectra of Porphyrins. *J. Mol. Spectrosc.* **1963**, *11*, 108–127.

(57) Liu, X.; Yeow, E. K.; Velate, S.; Steer, R. P. Photophysics and Spectroscopy of the Higher Electronic States of Zinc Metalloporphyrins: A Theoretical and Experimental Study. *Phys. Chem. Chem. Phys.* **2006**, *8*, 1298–1309.

(58) Tripathy, U.; Kowalska, D.; Liu, X.; Velate, S.; Steer, R. P. Photophysics of Soret-Excited Tetrapyrroles in Solution. I. Metalloporphyrins: MgTPP, ZnTPP, and CdTPP. *J. Phys. Chem. A* **2008**, *112*, 5824–5833.

(59) Tiwana, P.; Docampo, P.; Johnston, M. B.; Snaith, H. J.; Herz, L. M. Electron Mobility and Injection Dynamics in Mesoporous ZnO, SnO₂, and TiO₂ Films Used in Dye-Sensitized Solar Cells. *ACS Nano* **2011**, *5*, 5158–5166.

(60) Ai, X.; Anderson, N. A.; Guo, J.; Lian, T. Electron Injection Dynamics of Ru Polypyridyl Complexes on SnO₂ Nanocrystalline Thin Films. *J. Phys. Chem. B* **2005**, *109*, 7088–7094.

(61) Fajer, J.; Borg, D. C.; Forman, A.; Dolphin, D.; Felton, R. H. Pication Radicals and Dications of Metalloporphyrins. *J. Am. Chem. Soc.* **1970**, *92*, 3451–3459.

(62) Nayak, A.; Knauf, R. R.; Hanson, K.; Alibabaei, L.; Concepcion, J. J.; Ashford, D. L.; Dempsey, J. L.; Meyer, T. J. Synthesis and Photophysical Characterization of Porphyrin and Porphyrin–Ru(II) Polypyridyl Chromophore–Catalyst Assemblies on Mesoporous Metal Oxides. *Chem. Sci.* **2014**, *5*, 3115–3119.

(63) Inisan, C.; Saillard, J.-Y.; Guillard, R.; Tabard, A.; Le Mest, Y. Electrooxidation of Porphyrin Free Bases: Fate of the β -Cation Radical. *New J. Chem.* **1998**, *22*, 823–830.